# Exploring the Shallow Subsurface of Mars with the Ma_MISS Spectrometer on the ExoMars Rover Rosalind Franklin

M. C. de Sanctis, F. Altieri, E. Ammannito, S. de Angelis, B. Ehlmann, M. Ferrari, A. Frigeri, S. Fonte, M. Formisano, M. Giardino, et al.

The Planetary Science Journal, 3:142 (15pp), 2022 June https://doi.org/10.3847/PSJ/ac694f


# Exploring the Shallow Subsurface of Mars with the Ma_MISS Spectrometer on the ExoMars Rover Rosalind Franklin

M. C. De Sanctis[1], F. Altieri[1], E. Ammannito[2], S. De Angelis[1], B. Ehlmann[3], M. Ferrari[1], A. Frigeri[1], S. Fonte[1], M. Formisano[1], M. Giardino[2], A. Apuzzo[4], J. Brossier[1], N. Costa[1], L. Rossi[1], G. Vizzini[1], G. V. Ciarletti[5], and F. Westall[6]
[1] Institute for Space Astrophysics and Planetology, IAPS-INAF, via fosso del cavaliere 100, I-00133 Rome, Italy; mariacristina.desanctis@inaf.it
[2] Italian Space Agency, viale del Politecnico I-00133 Rome, Italy
[3] California Institute of Technology, 1200 E. California Boulevard, MC 150-21, Pasadena, CA 91125, USA
[4] Dip. Scienze, Università Roma Tre, L. go S.L. Murialdo 1, I-00146 Roma, Italy
[5] LATMOS, Univ. de Versailles St.-Quentin En-Yvelines, Guyancourt, France
[6] CNRS–Orleans, France
*Received 2022 January 24; revised 2022 April 15; accepted 2022 April 20; published 2022 June 16*

## Abstract

An essential part of the Exomars 2022 payload is the Mars Multispectral Imager for Subsurface Studies (Ma_MISS) experiment hosted by the drill system. Ma_MISS is a visible and near-infrared (0.4–2.3 $\mu$m) miniaturized spectrometer with an optical head inside the drill tip capable of observing the drill borehole with a spatial resolution of 120 $\mu$m. Here we report on how the Ma_MISS hyperspectral information provides in situ investigation of the subsurface at very fine resolution, prior to the collection of the samples that will be manipulated and crushed for further analysis by the analytical laboratory on the rover. Ma_MISS is the instrument that will closely investigate the subsurface mineralogical characteristics in its original geologic context at depths never reached before in Mars exploration. Ma_MISS recognizes all the major spectral features of the clays, basaltic, and minor phases expected at the ExoMars landing site, Oxia Planum. The high spatial resolution on the borehole wall is such that single grains of about 100 $\mu$m can be distinguishable in the assemblage of minerals observed by Ma_MISS. The spatial distribution of the mineralogies within the borehole walls is associated with the rocks and the processes that put these materials in place and possibly altered them with time, characterizing the habitats found in the stratigraphic record, indicating which ones are the most suitable to have held or to be holding nowadays traces of life.

*Unified Astronomy Thesaurus concepts:* Mars (1007)

## 1. ExoMars Mission

Mars is a primary destination to search for signs of life in our solar system, and the search for life is the aim of the most recent missions to the red planet, including ExoMars (ExoMars 2016 and ExoMars 2022). ExoMars 2016 consists of an orbiter, the Trace Gas Orbiter (TGO), and the entry, descent, and landing demonstrator module (EDM). The main scientific objective of TGO is to study in detail the atmospheric gases, including methane (CH4) and other minor components very difficult to detect (Allen et al. 2006; Sherwood Lollar et al. 2006; Yung et al. 2010), and observe the surface to hunt for signs of possible active processes.

ExoMars 2022 mission is composed of a lander and a rover. The lander is equipped with instruments devoted to atmospheric and geophysical investigations, while the rover includes a drill to collect samples and has a complex payload able to conduct detailed investigations of composition, search for organics, and recognize indicators of past or extant life (Vago et al. 2017). The drill is a critical element of the mission, as it will penetrate the Martian terrain and collect samples down to 2 m of depth. These samples are extremely important for a "life search" investigation because they are protected from the environmental conditions present at the surface, where radiation and oxidants can destroy organic compounds as demonstrated experimentally by Kminek and Bada (2006). Access to the Martian subsurface is needed to understand the nature, timing, and duration of alteration and sedimentation processes on Mars, as well as habitability conditions.

An essential part of the payload is the Mars Multispectral Imager for Subsurface Studies (Ma_MISS) experiment hosted by the drill system (De Sanctis et al. 2017). Ma_MISS is a visible and near-infrared (VNIR) miniaturized spectrometer with an optical head inside the drill tip capable of observing the borehole from where samples are collected. The search for biosignatures (likely fossil) requires a well-defined strategy (Vago et al. 2017) for which Ma_MISS is a key instrument. In achieving such a strategy, Ma_MISS provides an essential characterization of the mineralogy of the excavated borehole from which the samples are collected at different depths (between 0 and 2 m).

It is clear that other processes may also affect the preservation of organics in the subsurface. For example, dry sediment containing organics is less affected by radiation effects than wet materials (Makarov & Ponomarev 2017). On the other hand, near-surface processes involving changes in groundwater levels or the circulation of oxidizing waters would have a negative effect on the preservation of subsurface organics. Nevertheless, access to the Martian subsurface is needed to understand the nature, timing, and duration of alteration and sedimentation processes on Mars, as well as habitability conditions.

The collected samples will be introduced into the Analytical Laboratory Drawer (ALD) for a detailed analysis. However, once samples are crushed and prepared for the observations

into ALD, they will lose their original nature in terms of grain size, matrix, and texture, and any stratigraphic structure will be dismantled. The Ma_MISS spectrometer acquires spectra in the 0.4–2.3 $\mu$m range with a spectral sampling of about 20 nm, while the spatial resolution over the target is 120 $\mu$m. Making use of the drill's vertical and angular shaft motion, Ma_MISS can scan the borehole walls, building hyperspectral images. Ma_MISS spectral characteristics and fine spatial resolution enable the investigation of rocks in situ, prior to collection of the samples that will be manipulated and crushed before further analysis by the analytical laboratory. Thus, Ma_MISS is the instrument that will closely investigate the subsurface mineralogical characteristics of Mars's subsurface in its original geologic context.

## 2. Mars Mineralogy and Oxia Planum

### 2.1. Mars Mineralogy

The distinctive feature of Mars is the reddish hue of the surface, due to ferric oxides and oxyhydroxides present in Mars dust (e.g., Singer 1982). This fine-grained (<5 $\mu$m) dust is ubiquitous on the surface of Mars and covers large portions of the planet. Nevertheless, under the dust cover there are bedrock and sediments of distinctive composition, as large volcanic provinces composed of basalt and hydrated (OH, $H_2O$) deposits, with possible traces of other alteration minerals (e.g., Banin et al. 1992; Soderblom 1992). Silicate (ortho- and clino-pyroxenes, olivines, plagioclases and alkali feldspars), oxides (magnetite, hematite and ilmenite), hydroxides (goethite and akaganeite), sulfides (pyrrhotite and pyrite), carbonates, chlorides, and perchlorates have been identified (Ehlmann & Edwards 2014). Moreover, several hydrous phases have been detected, including clays (other hydrated silicates) and sulfates.

Hydrous minerals are of paramount importance for the life search, and Oxia Planum has been chosen as the landing site for ExoMars primarily because of the occurrence of a very large exposure of clay minerals (Carter et al. 2016; Mandon et al. 2021; Brossier et al. 2022) in association with carbonates (Brossier et al. 2022). Clays on Mars were mainly identified by orbital missions with the Observatoire pour la Minéralogie, l'Eau, les Glaces et l'Activité (OMEGA/Mars Express; Bibring et al. 2004, 2006) and Compact Reconnaissance Imaging Spectrometer for Mars (CRISM/MRO; Murchie et al. 2007, 2009) VNIR spectrometers, which detected regional phyllosilicate deposits (e.g., Poulet et al. 2005) and numerous smaller phyllosilicate-rich areas scattered throughout the ancient crust (e.g, Mustard et al. 2008). The observed distribution of hydrous phases implies that water–rock interaction was spatially extensive during the early history of Mars. Different varieties of clay minerals have been detected, such as smectites, kaolins, chlorites, and illite/mica (e.g., Mustard et al. 2008; Ehlmann et al. 2009). Smectites (e.g., saponite, montmorillonite, nontronite) are the main types of phyllosilicate observed on Mars from orbit (Ehlmann et al. 2011a; Carter et al. 2013). OMEGA identified primarily these hydrous minerals: Fe/Mg-rich phyllosilicates (nontronite and saponite), Al-rich smectites (montmorillonite and beidellite) and Al-kaolins, and hydrated sulfates. Other hydrous minerals identified are sulfate salts, and hydrated silica (e.g., Gendrin et al. 2005; Arvidson et al. 2005; Poulet et al. 2005; Milliken et al. 2008). CRISM revealed other phases, such as hydroxylated phyllosilicate prehnite, zeolites, carbonates, serpentines, and hydrated silica (or opaline; e.g., Milliken et al. 2008; Mustard et al. 2008; Ehlmann et al. 2009; Poulet et al. 2009; Murchie et al. 2009; Ehlmann et al. 2011a, 2011b). The hydroxylated sulfates jarosite and alunite were detected, as well as hydrated sulfates (including bassanite and gypsum; e.g., Wang et al. 2016 and references therein).

Hydrous minerals show a near-infrared spectrum dominated by features associated with either $H_2O$ or the OH group. $H_2O$ is either adsorbed at the crystal surface or absorbed in the interlayers present in most hydrous silicates (H-bonded to the lattice and/or with other interlayer water molecules). Water induces absorption bands in the 1.35–1.55 $\mu$m, 1.85–1.98 $\mu$m, and 2.70–2.85 $\mu$m regions. OH is found in the crystal structure of most hydrous minerals and exhibits a stretch transition in the 1.35–1.55 $\mu$m region and a number of additional diagnostic bands in the 2.14–2.65 $\mu$m region owing to vibrations of the X–OH bond (where X is a structural cation, typically $Mg^{2+}$, $Fe^{3+}$, $Fe^{2+}$, $Al^{3+}$, or $Si^{4+}$).

For this reason, phyllosilicates have been identified on Mars primarily by the presence of metal–OH absorptions at wavelengths centered between 2.2 and 2.4 $\mu$m (Hunt 1977; Clark et al. 1990; Bishop et al. 2013). The position of the bands shifts according to the cation–OH, and also the overall spectra change accordingly. Normally, the band minima in Al–OH smectites occur at shorter wavelengths (~2.2 $\mu$m), followed by Fe–OH band minima at longer wavelengths (~2.28 $\mu$m), while Mg–OH shows the minima at longer wavelengths (~2.31 $\mu$m). Chlorites exhibit bands that are wider and at longer wavelengths than smectites (~2.35 $\mu$m), and the kaolin group minerals (e.g., kaolinite, halloysite) are characterized by a clear doublet near ~2.2 $\mu$m and near ~1.4 $\mu$m that make them distinct from smectites. Most serpentines exhibit diagnostic absorptions at ~1.4 and ~2.32 $\mu$m.

Bound water in zeolite results in spectra dominated by a large shoulder between 2.3 and 2.4 $\mu$m, a sharp symmetrical absorption near 1.9 $\mu$m (similar to or sharper than that of phyllosilicates), and a small absorption near 1.4 $\mu$m. Smaller absorptions at ~1.2 and ~1.8 $\mu$m and in the right wing of the 1.9 $\mu$m band within the 2.2–2.4 $\mu$m range can be occasionally identified. These absorptions are due not only to water but also to metal–OH bonds with cations Al, Fe, Mg, Ca, and Na. Variations in NIR absorptions have been observed in laboratory reflectance spectra of terrestrial opals, and these spectral variations are inferred to represent differences in opal crystallinity/type.

Hydrated sulfates, hydrated carbonates, and hydrated salts in general also have their spectra dominated by water absorptions (Hanley et al. 2015; De Angelis et al. 2017, 2019).

Carbonates have many characteristic absorptions in the near-infrared range and typical absorptions in the 2.3–2.5 $\mu$m spectral region owing to X–$CO^{32-}$ vibrations (X being Mg, Fe, Na, or Ca; Gaffey 1987; De Angelis et al. 2019). More precisely, Mg-rich carbonates (magnesite) have paired absorptions at 2.30 and 2.50 $\mu$m, Fe-rich carbonates (siderite) at 2.33 and 2.53 $\mu$m, and Ca-rich carbonates (calcite) at 2.34 and 2.54 $\mu$m (Hunt & Salisbury 1971; Gaffey 1987). Like with phyllosilicates, positions of carbonate absorptions in this range depend on their composition.

From remote sensing, Mg and Ca sulfates (Liu et al. 2016) were identified in Valles Marineris, Meridiani Planum, and the northern polar region with OMEGA (e.g., Arvidson et al. 2005; Gendrin et al. 2005; Langevin et al. 2005) and CRISM

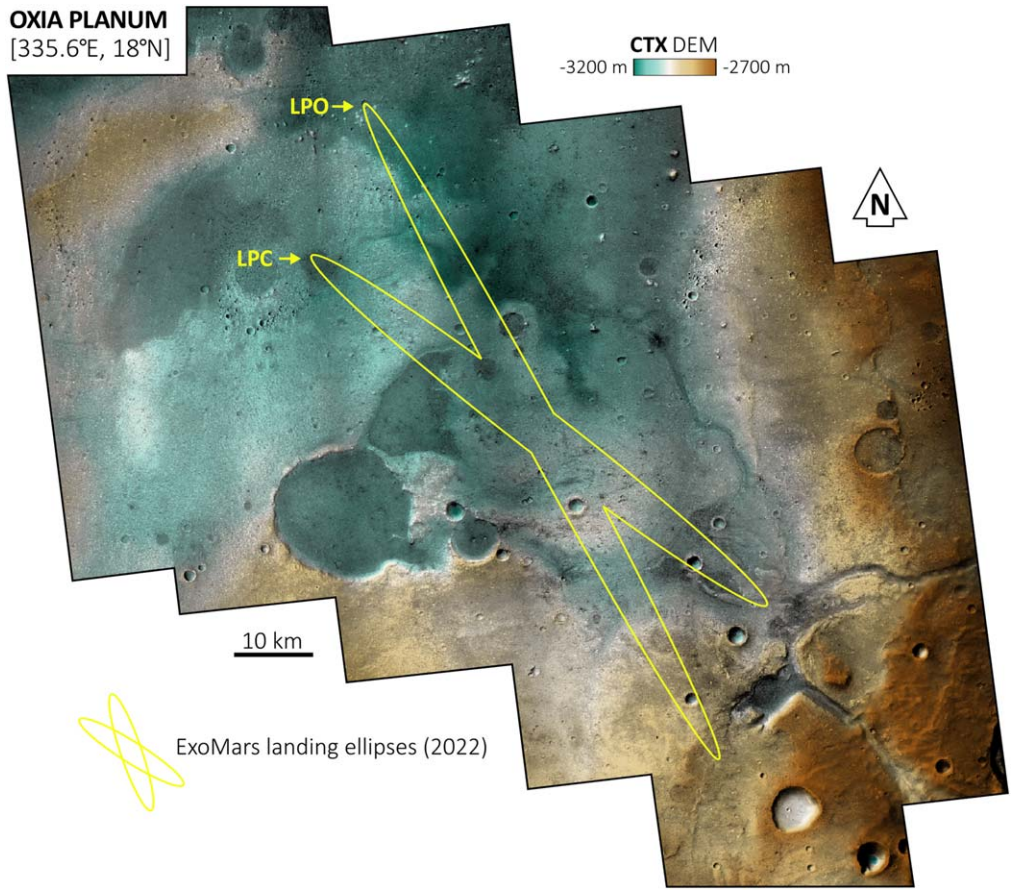


**Figure 1.** Oxia Planum (335.6°E, 18°N) and ExoMars (2022) landing site ellipses.

(e.g., Murchie et al. 2007) infrared data. Specifically, two important hydrous sulfates have been discovered on Mars by orbital remote sensing: monohydrated Mg sulfate ($MgSO_4 \cdot H_2O$), which was identified based on its distinct double absorption bands at 2.06 and 2.13 $\mu$m (Gendrin et al. 2005; Arvidson et al. 2005), and polyhydrated sulfate. The nature of the latter is largely undetermined owing to the fact that the spectral features match approximately with those of hydrous sulfates with a variety of cations and hydration degrees (Bibring et al. 2006, 2007). Other types of hydrated sulfates (Bishop et al. 2009; Lichtenberg et al. 2010), especially Fe sulfates (e.g., jarosite, hydroxylated ferric sulfates, and szomolnokite) and Al sulfates (alunite), have been found by remote sensing in low abundance and/or in localized small areas. Nevertheless, in situ measurements performed at all landing sites have revealed Mg, Ca, and $Fe^{3+}$ sulfates, either in outcrops or throughout the subsurface regoliths (e.g., McSween et al. 1999; Squyres et al. 2004; Wang et al. 2006; Arvidson et al. 2010; Kounaves et al. 2010; Vaniman et al. 2013).

### 2.2. Surface Mineralogy of Oxia Planum

Oxia Planum (Figure 1) was selected as the landing site of the ExoMars 2022 mission. This area is considered suitable to achieve the scientific objectives of ExoMars 2022 and safe in terms of risks concerning the landing. Oxia Planum is located at latitudes 16°–19° N and longitudes 23°–28° W, near the Martian crustal dichotomy border of Chryse Planitia (Figure 1). It is a relatively smooth and low-elevation terrain and is confined between Mawrth Vallis and Ares Vallis, two major outflow channel systems.

Spectroscopic data collected from the CRISM (Murchie et al. 2007, 2009) and OMEGA (Bibring et al. 2004, 2006) instruments, along with the imaging data gathered by the High Resolution Imaging Science Experiment (HiRISE; McEwen et al. 2007, 2010) camera, found evidence for a long-lasting aqueous history of this site during the Noachian age (Carter et al. 2016; Quantin-Nataf et al. 2021), showing an extensive distribution of clay-bearing terrains. This unit is located where Tanaka et al. (2014) reported units dating from early to mid-Noachian, older than 3.8 Ga (Quantin-Nataf et al. 2021). The bedrock unit identified in Oxia is one of the largest exposures of clays on Mars and belongs to a broader detection extending further westward in Arabia Terra and northward to Mawrth Vallis (e.g., Loizeau et al. 2007; Bishop et al. 2008; McKeown et al. 2009; Noe Dobrea et al. 2010).

The estimated thickness is more than 50 m (Quantin-Nataf et al. 2021). However, it is difficult to calculate the exact amount of clays in this region from the orbital data, and the origin of such large amounts of hydrated minerals is not yet fully understood. HiRISE data show that the clays-bearing unit is characterized by metric to decametric fractures (Mandon et al. 2021). Spectroscopic and imaging data suggest that the clay-bearing unit can be further subdivided into two subunits differing in fracture size, color, and spectral properties (Mandon et al. 2021). The first subunit always appears stratigraphically below the second one. It shows metric-scale fractures and appears reddish in HiRISE color images. This unit shows absorption bands at about 1.4, 1.9, 2.3, and 2.4 $\mu$m,

interpreted as typical of Fe/Mg-rich phyllosilicate (smectite clays, likely Fe/Mg-rich saponite, or smectite/mica, e.g., vermiculite; Carter et al. 2016). In some locations, an additional spectral absorption near 2.5 $\mu$m has been identified and suggests the presence of other phyllosilicate minerals or carbonates (Altieri et al. 2021; Mandon et al. 2021 Brossier et al. 2022). In contrast, the second unit appears above the first one, showing fractures in the tens of meters and a bluish tone, and displays weaker bands of clay minerals. Moreover, this subunit exhibits a 1 $\mu$m broad band, probably linked to the presence of olivine (Mandon et al. 2021; Brossier et al. 2022), in relation to an ancient fan delta at the outlet of the Coogoon Valles system in the eastern part of the landing site (Molina et al. 2017; Quantin-Nataf et al. 2021).

Rounded isolated buttes that overlie the clay-bearing unit have been identified (McNeil et al. 2021) and may also be related to aqueous processes occurring in the region. According to geologic mappings by Ivanov et al. (2020) and Quantin-Nataf et al. (2021), Oxia planum exhibits an unaltered mafic-rich dark resistant unit, likely of Amazonian age, that caps the other units and possibly originated from volcanism (e.g., lava flows or ash deposits). This unit exhibits a 1 $\mu$m broad absorption, probably linked to the presence of olivine and pyroxenes. The 1 $\mu$m broad absorption is found in correspondence of an ancient delta belonging to the fluvial system of Coogoon Valles in the eastern part of the landing site (Molina et al. 2017; Quantin-Nataf et al. 2021). Morphological features (such as inverted and shallow channels and degraded crater ejecta) and estimation of crater obliteration show evidence for intense erosion in Oxia Planum. Nevertheless, the emplacement and slow removal of the dark resistant unit indicate that many of the Noachian sediments in Oxia could have been preserved from the harsh Martian environment for a very long time, likely much of the time since they were emplaced (Quantin-Nataf et al. 2021).

Recent analysis of ExoMars 2022 landing site data (Brossier et al. 2022) demonstrates small variation in the minima of the 2.3 and 2.4 $\mu$m bands, suggesting an almost uniform spectral behavior of the clays outcrops at the spatial resolution of the orbital CRISM data available over the landing site ellipses. Nevertheless, the identification of the clay minerals is not straightforward, with the spectra being compatible mainly with Fe-rich saponite like Griffithite and/or smectite/mica like vermiculite (Mandon et al. 2021; Brossier et al. 2022), but also with the possible presence of nontronites and Al-rich clays and kaolins as minor components. In particular, Fe-rich saponites, which have characteristic absorptions near 1.40–1.42 $\mu$m, 2.30–2.32 $\mu$m, and 2.40 $\mu$m (Treiman et al. 2014), nicely match the band minima retrieved at Oxia, while nontronites (and Al-rich phases) have been clearly detected in the Oxia catchment area. It is reasonable to think that the spectra in Oxia are the result of a mixture of different species, including carbonates, serpentines, and/or chlorites (Mandon et al. 2021; Brossier et al. 2022). However, it is challenging to ascertain their presence since they have spectral absorptions occurring in the 2.3–2.5 $\mu$m range, similar to the clays (Brossier et al. 2022).

### 2.3. What Mineralogy is Expected in the Subsurface?

Ma_MISS will investigate deeper into the subsurface than prior rover missions (Figure 2). The two Viking landers and Phoenix landers scooped materials from the upper few centimeters of regolith for compositional analysis. The Mars Exploration Rovers (MER) used their wheels to excavate trenches up to 11 cm deep (Sullivan et al. 2011) and collected chemical and mineralogical compositional profiles with the alpha-particle X-ray spectrometer and Mossbauer instruments. Terrains excavated from the first centimeters showed high ferric sulfate contents or silica contents, likely signaling an influence from volcanic or hydrothermal processes (Gellert & Yen 2019; Morris et al. 2019). The MER rovers also had a rock abrasion tool (RAT) (Gorevan et al. 2003) that grounds up to 9 mm deep and revealed coatings enriched in S, Cl, Zn, and Ni and iron oxides on outer rock surfaces.

Mars Science Laboratory (MSL) drilled around 5 cm into multiple rocks, collecting powdered materials for analysis below any coatings. MSL rover successfully drilled 12 full-depth drill holes into the Martian surface and analyzed the sampled material using onboard instruments, giving us new insights into the potential habitability and geologic diversity of ancient Mars (Figure 3).

The samples acquired by MSL demonstrate differences between the surface and the subsurface, as shown in the colors of the excavated fines (Figure 3), mainly linked with the oxidation state of the materials. Drilled samples exhibit a range of gray and reddish colors that reflect mineralogical changes from alteration and fluid/rock interactions. The collected data show that the dust-coated surfaces and the soils are characterized by a strong positive reflectance slope in the visible range, commonly ascribed to the presence of iron oxides.

Ferric minerals normally show crystal field absorptions and a strong charge transfer band extending from the ultraviolet into the visible (Hunt & Ashley 1979). In particular, nanophase oxides, as hematite, do not show distinct crystal field bands, but the spectra have a strong iron-oxygen charge transfer absorption edge through the visible wavelengths (Morris et al. 1989). The Martian spectral slope is consistent with the presence of nanophase iron oxides, able to give the reddish color to weathered Martian surface materials (Morris et al. 1993, 1997; Wellington et al. 2017). Conversely, fresh surfaces, such as powders produced by the drill tool, are normally grayer in visible wavelengths than their reddish dust surfaces. Nevertheless, their visible spectra vary considerably between the different drilled sites. The samples studied by MSL demonstrated that the Gale crater has experienced a rich and diverse aqueous past with the first in situ identification of tridymite, gypsum, and dioctahedral smectite on the Martian surface (Morris et al. 2016; Bristow et al. 2018; Vaniman et al. 2018). Most interesting is the fact that well-preserved organic material was discovered at Pahrump Hills (Confidence Hills and Mojave 2), even with the very harsh surface conditions, suggesting that even better preservation may be possible farther beneath the Martian surface (Eigenbrode et al. 2018).

Differently from the previous missions, the ExoMars drill and Ma_MISS measurements will be the deepest compositional measurements made on Mars up to 2 m depth. Over the 2 m ExoMars is expected to drill, Ma_MISS can detect compositional gradients with depth. Changes in type and abundance of minerals, weathering fronts or rinds, and diagenetic veins or nodules will be mapped as a function of depth. The spectral range of Ma_MISS is optimal to detect changes in the occurrence and crystal chemistry of olivines and pyroxenes, as well as Fe(II)/Fe(III) in silicates, oxides, and salts, using the spectral range from 0.4 to 2.3 $\mu$m, which is sensitive to crystal

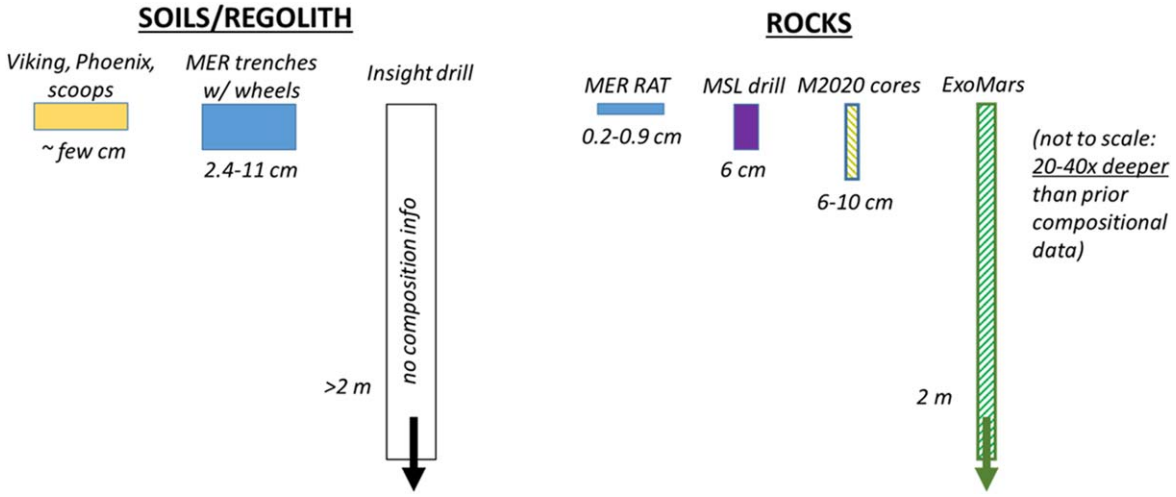


**Figure 2.** Representation of the drill/scoop/trench depths planned and realized by previous Mars missions in comparison with ExoMars. ExoMars drill excavation depth is not to scale.

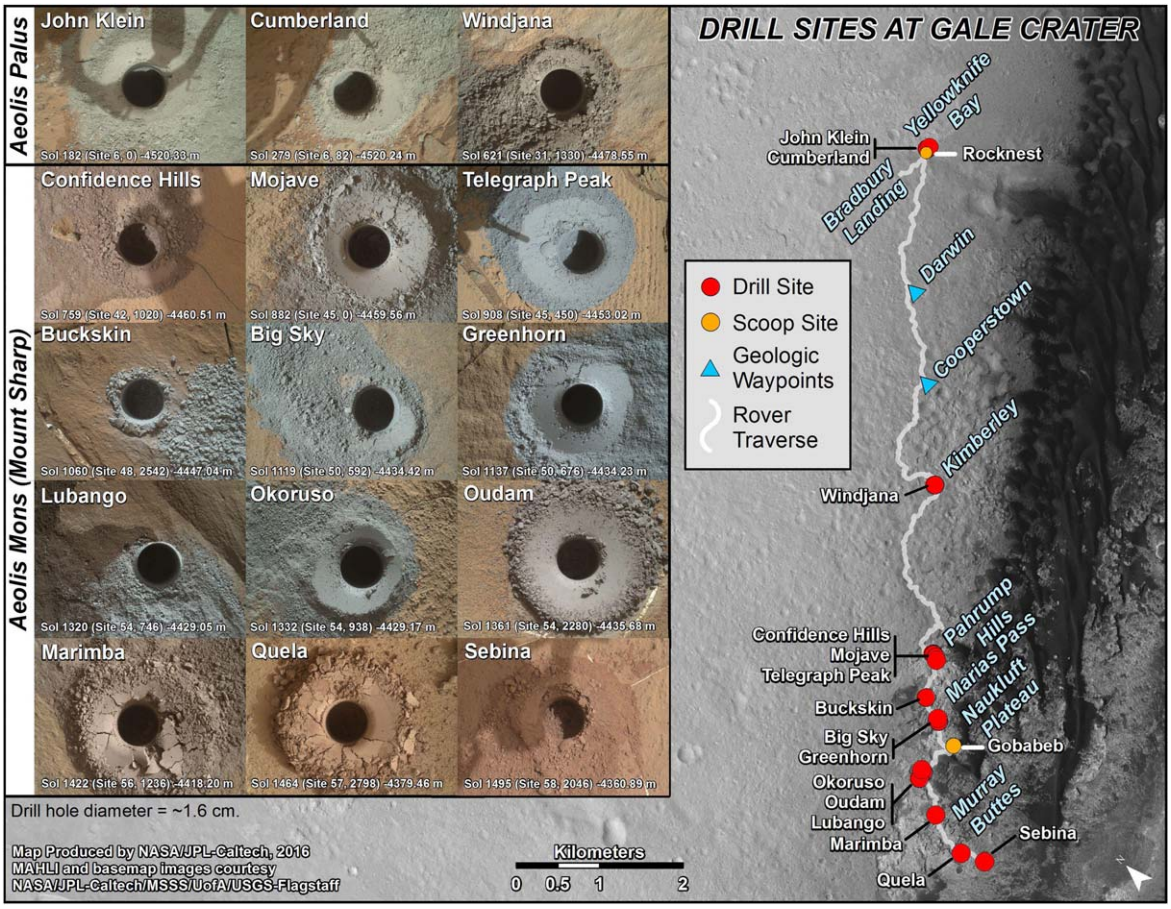


**Figure 3.** The map of the location of NASA's Curiosity's first 19 rock sampling sites. The samples have been analyzed by laboratory instruments inside the vehicle. On the left, 15 images of the drilled holes show the variation in color and grain size of cuttings and powders. Inset: MAHLI images of all full-depth drill holes taken at a standoff of 10 cm with the exception of Sebina, which was taken at a standoff of 25 cm. Image Credits: NASA/JPL-Caltech/MSSS/UA (PIA21254). The image does not represent all the drilled rocks. In 2021 September, a total of 33 similarly heterogeneous-appearing drill samples have been collected (MSL update to MEPAG VM #13, 2021).

field transitions and charge transfer absorptions (e.g., Rossman & Ehlmann 2019).

There may be changes in these redox-sensitive minerals with depth that record different environments. As an example, within Gale crater's Mt. Sharp, Curiosity recorded sets of strata enriched in hematite (Fe(III) oxide) contrasting with earlier strata enriched in magnetite (Fe(II) oxide) that have been hypothesized to represent gradients between oxidizing and reducing fluids, perhaps driven by changes in the redox state of the Martian atmosphere (Hurowitz et al. 2017). Additionally, strata high up Mt. Sharp have Fe(III) nontronite, a dioctahedral smectite, as well as occasional jarosite, which contrasts with

Fe(II) saponite, a trioctahedral smectite, in lower strata, hypothesized to reflect top-down weathering from briny fluids (Bristow et al. 2018). If found at Oxia, such changes will be recognized by changes in electronic transition absorptions and the metal–OH absorption near 1.4 $\mu$m.

Changes in the hydration state of materials have also been observed with depth on Mars, with uppermost surfaces more desiccated than interiors. Calcium sulfates at Gale crater are of variable hydration state: gypsum, $CaSO_4 \cdot 2H_2O$; bassanite $CaSO_4 \cdot 0.5H_2O$; anhydrite $CaSO_4$; and dehydrate with processing (Vaniman et al. 2018). Hydrated silica phases have been observed to dehydrate with sampling and processing (Rapin et al. 2018). Thus, Ma_MISS observations are the best measurements to characterize the materials through the 1.4, 1.9, and 2.2 $\mu$m absorptions (Anderson & Wickersheim 1964).

Water ice, if present, is also detectable by Ma_MISS from its 0.94, 1.5, and 2.0 $\mu$m absorptions. Numerical models (e.g., Formisano et al. 2021) suggest that Oxia Planum surface temperatures can vary in the range 175–270 K, depending on the thermal inertia of the site, still compatible with the presence of water ice and hydrated phases. Nevertheless, drilling activity can strongly influence the thermal environment of the Martian surface and shallow surface, in particular the layers near the borehole in contact with the drill tip and rods. Establishing the heat released by the drill operations becomes critical since it could compromise the survival of volatile species in the subsurface (Formisano et al. 2021). The increase in temperature due to the drilling operations ranges from about 55 to 120 K (Formisano et al. 2021), depending on the assumed frictional coefficient and rotational speed of the drill. Given the possible thermal scenarios explored by Formisano et al. (2021), assuming the existence of a body of ice (a water-ice spherical deposit with radius equal to the drill tip length), in the coldest case explored, the fraction of the initial mass of this deposit remaining after 90 minutes is about 60%. On the contrary, in the warm and hot cases, only a negligible fraction of ice is retained.

The effects of the presence of ice on the drill activity have been reported by Zacny & Cooper (2006), showing two scenarios. In the first one, the drilling takes place in water-rich areas where pressures are below the triple point of water. In this case, most of the heat generated by the drilling operations will be used to sublimate ices that will blow the drilled cuttings from the bottom of the hole, cleaning the hole. In the second one, the drilling takes place in water-bearing formations where the pressures are above the triple point. Here the water, also present as liquid, could refreeze and trap the bit inside the hole.

The presence of water ice, hydrated minerals, or volatiles at low latitude cannot be completely ruled out. Wilson et al. (2017) discovered hydrogen-rich areas at low and equatorial latitudes, in the reconstruction of the Mars Odyssey Neutron Spectrometer (MONS) data, in the Medusae Fossae Formation, and on the western slopes for the Tharsis Montes and Elysium Mons. This would imply the presence of buried water ice.

However, the presence of large amounts of water ice in the subsurface at Oxia is not expected, given the latitude of Oxia, and the simulations for the ice preservation, as well as the implication for the drill activity, are somehow extreme.

In the case of Oxia, the study of the subsurface could provide information on depositional regimes in zones not too far from the delta deposits. In particular, the granulometric variation with depth will highlight the presence of layers and laminations whose bedding and dip can be determined by Ma_MISS through measurements on several drillings. This will help to reconstruct the paleoenvironments that have characterized Oxia Planum.

In addition, at sufficient concentrations, organic molecules will also be detectable (Ferrari et al. 2021): depending on the kind of organic, the Ma_MISS instrument is capable of detecting their presence even with a 1 wt.% in the mixture, as verified by specific tests in the laboratory using the Ma_MISS breadboard model on mineral/organic mixtures in different proportions. Spectroscopic measurements collected on these mineral/organic mixtures are useful to understand how the Ma_MISS instrument can detect traces of organics intimately mixed with minerals that could be present in sedimentary sequences or in hydrothermal products in the Martian subsurface, which is one of the main scientific objectives of the ExoMars 2022 mission.

## 3. Ma_MISS Description

### 3.1. Ma_MISS Instrument

The Ma_MISS miniaturized spectrometer is hosted inside the drill system of the ExoMars 2022 rover and will characterize the mineralogy and stratigraphy of the excavated borehole wall at different depths (up to 2 m). Ma_MISS is a modular instrument, and it consists of two main parts: (i) the spectrometer with the proximity electronics located outside of the drilling tool, and (ii) the optical head and fibers located inside the drill itself (De Sanctis et al. 2017; see Figure 4 and Table 1).

The drill consists of a main rod of 2.5 cm in diameter, which hosts the drill tip, plus three additional rods (each 50 cm long), which allow it to reach a maximum depth of 2 m. The drill tip also has the Ma_MISS optical head (OH) and a sapphire window with high hardness and transparency, allowing us to observe the borehole wall. All the rods are equipped with optical fibers, able to transmit light and signal. The first extension rod is connected to the nonrotating part of the drill, hosted on the rover, separated through a fiber optical rotating joint (FORJ), which permits the continuity of the signal link between the rotating part of the drill and the spectrometer.

The OH consists of an Illumination Relay System (IRS) and a Signal Relay System (SRS). It is constituted of several miniaturized metallic mirrors to couple light from illumination fiber (IRS) and the signal coupling mirror system (SRS). With Illumination Offner Relay, the light coming from the IRS impinges the main mirror and is reflected to the secondary mirror, then again to the main mirror, and finally to the folding mirror. The light reflected from Mars's surface is collected by the Signal Offner Relay. It passes through the sapphire window, impinges the folding mirror, and is reflected to the main mirror, then to the secondary, back to the main, and, finally, it is collected by the optic fiber.

Ma_MISS is equipped with a light source of 5 W to illuminate the borehole. The light is carried through the optical fibers to the miniaturized optical head and from this, through the sapphire window, illuminates the borehole. The illumination spot on the target is about 1 mm in diameter at a focal distance of about 0.6 mm. The reflected signal is fed, through the sapphire window, to a collimator and carried by the optical fibers to the spectrometer outside of the rods. The reflected light is collected through a 120 $\mu$m spot (defining the spatial resolution). Ma_MISS also has a

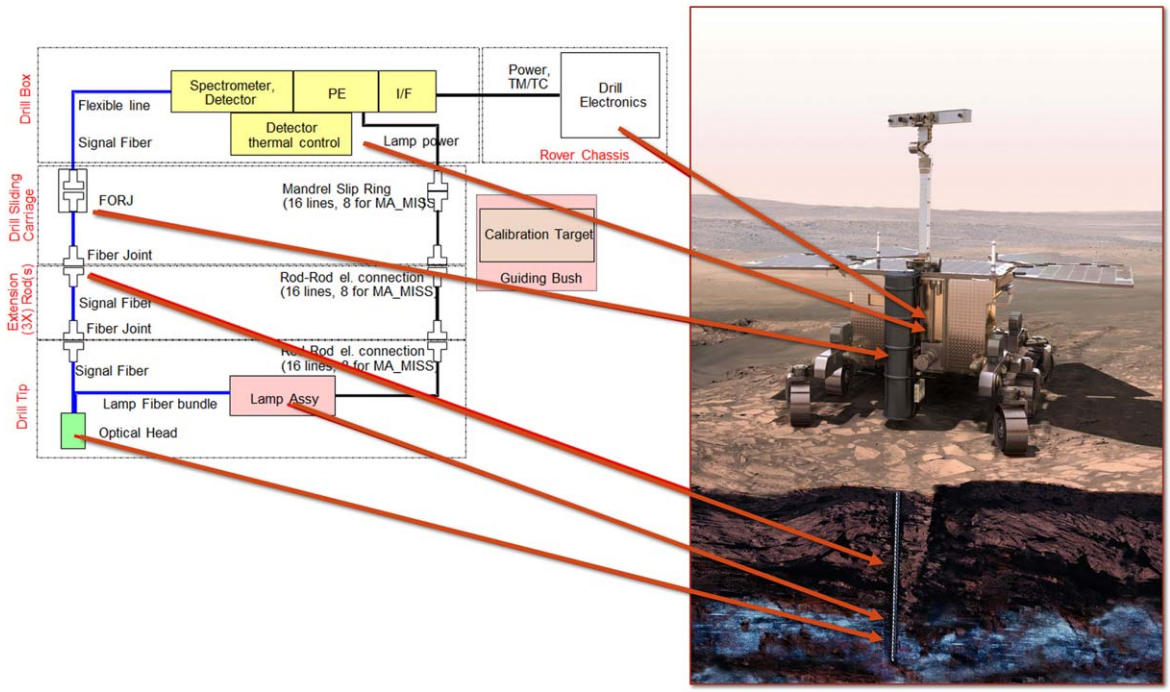


**Figure 4.** Schematic view of Ma_MISS instruments with the different parts in the rod/tip and on the drill box.

**Table 1**
Ma_MISS Main Characteristics

| Ma_MISS Main Characteristics | |
|---|---|
| Spectral range | 400–2300 nm |
| Spectral sampling | 5.3 nm |
| Spectral resolution FWHM | 37 nm (<1000 nm) // 17–23 nm (>1000 nm) |
| Number of spectral channels | 364 |
| Expected S/N | >102 |
| Focal distance | 0.6 mm |
| Spatial resolution o (signal fiber core diameter) | 120 $\mu$m |
| Fiber F/# | 2.2 |
| IFOV | 120 $\mu$m |
| Spatial sampling (min.)* | 112 $\mu$m |
| Spectrometer | Modified Offner configuration |
| Focal plane | HgCdTe Sofradir detector |
| | Window: 256 × 500 pixel |
| | Active window: 5 × 364 pixel |
| | Pixel size: 30 $\mu$m |
| | Dark current: <3pA @223K |
| Light source | Tungsten halogen lamp (5 W) |
| Mass | 0.87 kg |
| Power consumption (peak) | 22.8 W (0°C) |

**Note.** An asterisk denotes that the spatial sampling is defined by the drill rotation angular step.

calibration target with four different sectors to validate the spectral and radiometric response when on Mars (for details see Tinivelli et al. 2018). The calibration target is placed inside the drill box, close to the hole through which the drill tip protrudes; in this way calibration can be carried out before any drill campaign. The target is a small circle with sectors reporting well-characterized painting and spectral features, to check both radiometric and spectral behavior of Ma_MISS. Four different material/coatings, with suitable spectral reflectivity levels, are used: one for spectral calibration and three for radiometric calibration within the dynamic range of the instrument.

#### 3.1.1. Ma_MISS Operative Modes

The spectrometer observes a single point target on the borehole wall subsurface and, using the drill movements, can build up spectral images of the target. The spatial resolution of Ma_MISS on the borehole is always the same and corresponds to 120 $\mu$m. The borehole vertical datum is set from the drill's telemetry, setting the distance reference when advancement of the tip is hindered by the first contact with the ground.

Depending on the expected features of interest, the observation window can scan the subsurface by means of drill tip rotation or translation, thus providing ring or column hyperspectral images (Figure 5). By combining several column and ring observations, Ma_MISS allows the reconstruction of a fairly complete image of the borehole wall (Ferrari et al. 2022). The ring can be obtained by combining the acquisition of $N$ points with angular separation $\Delta\theta$, in coordination with the drill. The maximum number of different points that can be acquired on a ring depends on drill angular resolution. The drill minimum angular resolution (step) is $0\overset{\circ}{.}47$, corresponding to a maximum of 765 points of Ma_MISS on a ring. Concerning the columns, the standard column acquisition is the acquisition of $N$ points with vertical separation $\Delta z$, in coordination with the drill. The minimum step $\Delta z$ between two points in the column is <2 mm.

Ma_MISS can acquire data with different integration times, according to expected albedo of the features of interest. To increase the signal-to-noise ratio (S/N), Ma_MISS electronics is able to acquire from 1 to 256 spectra on a single spot, using an integration time of several milliseconds, averaging them to reduce the noise associated with the measures. In this way, we have estimated that an S/N > 100 is easily obtained also in the case of low-albedo materials. It must be also recalled that the borehole is illuminated by the Ma_MISS lamp; thus, Ma_MISS

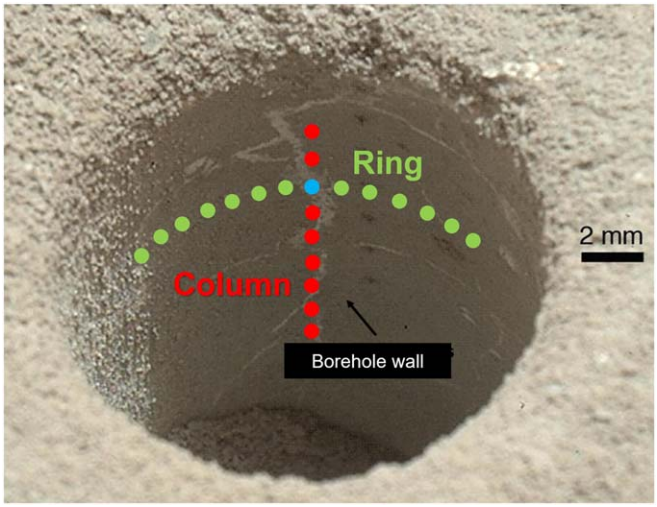


**Figure 5.** Schematic representation of the Ma_MISS acquisition modes on the borehole wall. The ring images are acquired using the drill rotation, while the column images are taken using the vertical translation of the drill. The image of the borehole is adapted from https://photojournal.jpl.nasa.gov/catalog/PIA17594.

acquisition conditions do not depend on natural light conditions.

The Ma_MISS spectral range and sampling capabilities have been carefully selected to allow the study of minerals in situ before the collection of samples, determining the composition of subsurface materials and mapping the distribution of the different phases (see Table 1). The layer thickness and scale within the stratigraphic column, combined with the composition of each layer, will give important clues about the sedimentary/geological processes that took place at the landing site. These are essential information to understand the nature of the samples that, later, will be analyzed by the analytical laboratory on the rover.

Several tests have been done on the capability of Ma_MISS to observe the borehole walls during the drilling activity, concerning the possible dust accumulation on the window. From the tests done in the laboratory, it turns out that dust affects spectral identification only if several microns of dust are accumulated on the window. However, we must consider two factors that do not permit dust accumulation on the window: (a) gravity and movement (the window is in vertical position and continuously moved thanks to the drill movements), and (b) the presence of a small brush that cleans the window and furthermore helps in removal of the possible dust accumulated on it.

The Ma_MISS window is made of an extremely hard and resistant material (sapphire), and the test done on it confirmed that it is extremely resistant to scratches and abrasions. The drill with the Ma_MISS window has been tested in several different conditions and on different rocks and materials, without reporting any issues on the hardness of the window.

### 3.2. Ma_MISS Laboratory Breadboard

In order to verify the Ma_MISS capabilities and to optimize the scientific interpretation of the collected data, a laboratory breadboard (BB) of the instrument has been extensively used in past years (Figure 6). Many different measurements have been carried out on the Ma_MISS BB, including spectral acquisitions of rocks and minerals expected to be present at the landing site (De Angelis et al. 2014, 2015). Spectra have been acquired on many anhydrous and hydrated silicates, phyllosilicates, carbonates, oxyhydroxides, sulfates, and phosphates and on a selection of organic compounds.

The breadboard setup (BB) is in use at the Istituto Nazionale di Astrofisica (INAF), specifically in the Istituto di Astrofisica e Planetologia Spaziali (IAPS) laboratory (described in detail in De Angelis et al. 2014), and it consists of the main optical subsystems of the Ma_MISS instrument except for the spectrometer. The optical system is made of different parts: (1) an illumination source (miniaturized lamp) of 5 W integrated within the instrument, and (2) a bundle of optical fibers that carries the light from the lamp to the optical head, which consists of several miniaturized mirrors and acts to focus the light on the external target. The light is focused through a sapphire window on the target, at a distance of 0.6 mm; then, the scattered light is recollected by the same optical head, and an optical fiber carries the signal to a spectrometer. In this setup, the breadboard is coupled with a FieldSpec Pro, which operates in the 0.35–2.5 $\mu$m range with a spectral sampling of 1 nm and by a spectral resolution of 3–8 nm. FieldSpec Pro is a commercial spectrometer that uses three different detectors to cover the 0.35–2.5 range, while Ma_MISS has only one detector to cover its spectral range.

The Ma_MISS instrument is instead characterized by a spectral sampling of 5 nm and a spectral resolution >20 nm, with the operative range 0.4–2.3 $\mu$m. Given the differences, in terms of spectral characteristics, between the Ma_MISS flight model and the laboratory breadboard, the acquired spectra were thus (i) restricted to the Ma_MISS flight model nominal range, (ii) resampled to Ma_MISS flight model sampling of 5 nm, and (iii) convolved with Ma_MISS flight model spectral resolution. In particular, for the convolution, a Gaussian spectral response function was used as a kernel, with varying FWHM equal to 37 nm (0.5–1 $\mu$m range), 24 nm (1–1.5 $\mu$m range), and 20 nm (1.5–2.3 $\mu$m range) according to the on-ground calibration results.

A selection of spectra of phyllosilicates acquired with the breadboard and resampled as described is shown in Figure 7. Spectra are characterized by a large variety, with $H_2O$-bearing minerals characterized by various degrees of hydration (absorption bands at ~1.4 and ~1.9 $\mu$m), OH-bearing minerals (band at ~1.4 $\mu$m), samples with variable Fe(II)/Fe(III) content (features in the range 0.5–1 $\mu$m), or samples characterized by the presence of different metal–OH absorptions in the 2.1–2.3 $\mu$m region.

Conversely, Ma_MISS limited spectral range in the IR is such that minerals having main absorptions at wavelengths longer than 2.3 $\mu$m are not easily recognized, using the characteristic features present in their spectra beyond 2.3 $\mu$m. At the same time, it must be considered that, given the high spatial resolution of Ma_MISS, it is conceivable that Ma_MISS will observe grains of monominerals, enhancing the capability to distinguish different phases, as demonstrated by previous measurements on natural samples (De Angelis et al. 2017). For instance, distinguishing between carbonates and the most common clays (both with bands near 2.3 $\mu$m and beyond) can be obtained thanks to the absence (carbonates) and presence (clays) of the 1.4 and 1.9 $\mu$m absorptions, plus additional bands typical of the different minerals (Figure 8).

Distinguish between Fe and Mg smectites is more difficult because the metal–OH combination bands shift systematically

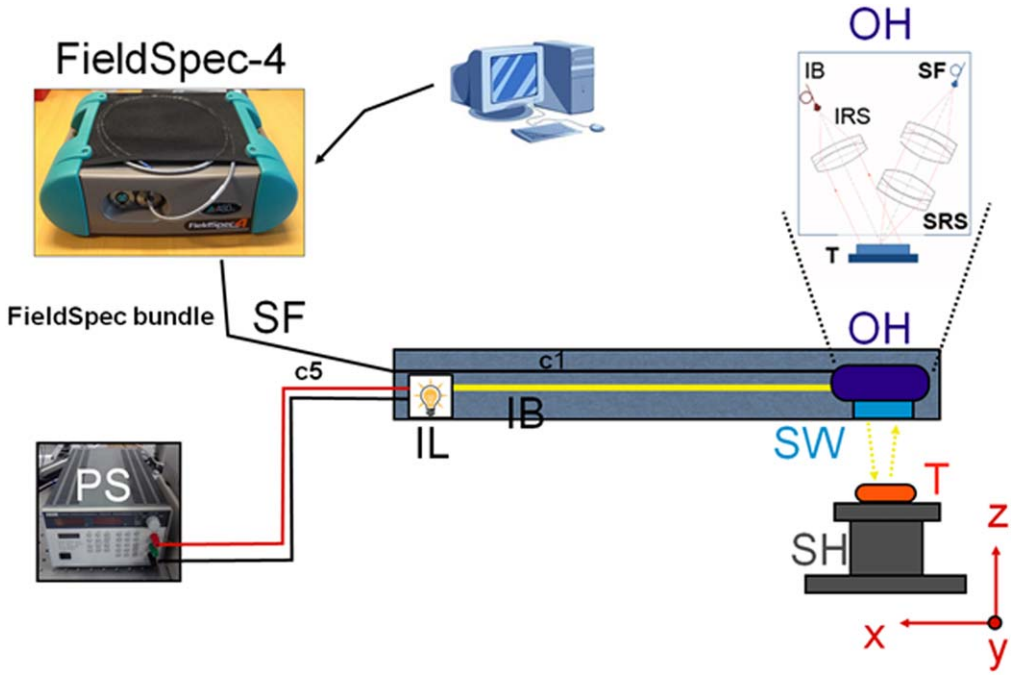


**Figure 6.** The laboratory model (breadboard) of the instrument includes all the subsystems: the illumination system (IL), consisting of the 5 W lamp and the illumination bundle; the optical head (OH); the sapphire window (SW); the signal fiber (SF) (signal link), which is a series of three optical fibers that carry the collected light from the optical head to the laboratory spectrometer (FieldSpec). Power Supply (PS) and Sample Holder (SH) and the test sample (T) are also illustrated in the diagram.

between 2.32 $\mu$m (Mg2+) and 2.36 $\mu$m (Fe2+) with Fe–Mg content, and the minima of these absorptions are beyond the Ma_MISS range. However, the 1.4 $\mu$m band is also affected, and a shift in the 2.3 $\mu$m band corresponds to a shift in the 1.4 $\mu$m band (Chemtob et al. 2015). Thus, even if difficult, the combinations of the absorptions and the high spatial resolution can give an indication of the nature of the clays (Figure 8(b)), as demonstrated by the measurements done with the Ma_MISS breadboard here reported.

## 4. Natural Rocks and Synthetic Targets Observed during Ma_MISS Calibration Campaign

During the Ma_MISS calibration campaign, laboratory measurements were performed on different minerals and rocks that can be considered as Mars analogs with the aim of characterizing the scientific performance of the Ma_MISS flight spectrometer. Moreover, we also checked the Ma_MISS capability to recognize spectral features when the drill rods are mounted.

### *4.1. Tests on Rocks and Synthetic Targets without the Extension Rods*

Part of the characterization of the scientific performances of the Ma_MISS instrument was made in 2018 April, at the Leonardo calibration facility in Florence (Italy). During this activity, the Ma_MISS spectrometer was inside a thermo-vacuum chamber (TVC) to maintain the detector unit at the operating temperature TDet = −50°C. The setup also included the ground support equipment, the tip, the drill tool, the optical head with the illuminating system, the optical fibers with the FORJ, and the mini-AVIM connection adapters to pass the signal inside the TVC. After having performed the spectral and radiometric calibration, we did some performances/characterization tests using the FM Calibration Target, synthetic targets, and natural samples. For all these tests, we used only the Ma_MISS tip, without any further extension rod.

During the characterization phase, we selected three natural samples: (1) a slab of dunite rock, (2) a slab of Montiferru (Bonàrcado) vescicular basalt, and (3) a slab of gypsum. Those samples have been selected because they have clear absorption bands in the Ma_MISS spectral range, because they are representative of mineralogies that we could expect in the Martian subsurface, and also because they have been fully characterized by previous spectral and petrological analysis.

All the samples were mounted on an ad hoc sample holder (Figure 9) screwed on a guide to permit micrometric movement, which was necessary to reach the focus position or to illuminate specific features of interest on the selected sample. These samples have been spectrally characterized in the INAF laboratory, using a FieldSpec4 spectrometer, and the spectra obtained in INAF have been used as references. The two spectrometers, Ma_MISS spectrometer and FieldSpec4, have different spectral range and resolution, as well as different field of view (FOV), that make the comparison between the spectra acquired with Ma_MISS and FieldSpec4 not straightforward. In particular, the different spatial resolution of the two instruments (Ma_MISS has 0.12 mm and FieldSpec4 has 6 mm) can lead to collecting quite different spectra when analyzing heterogeneous samples (De Angelis et al. 2017). In addition, the FieldSpec4 has a better spectral resolution (3–8 nm) with respect to the Ma_MISS spectrometer (about 20 nm). Another important difference between the two instruments is that Ma_MISS uses a 5 W miniaturized lamp to illuminate the sample, while the FieldSpec4 setup includes a 100 W Quartz Tungsten Halogen lamp as a light source.

The comparison between the data acquired with Ma_MISS FM during the calibration and those acquired at the

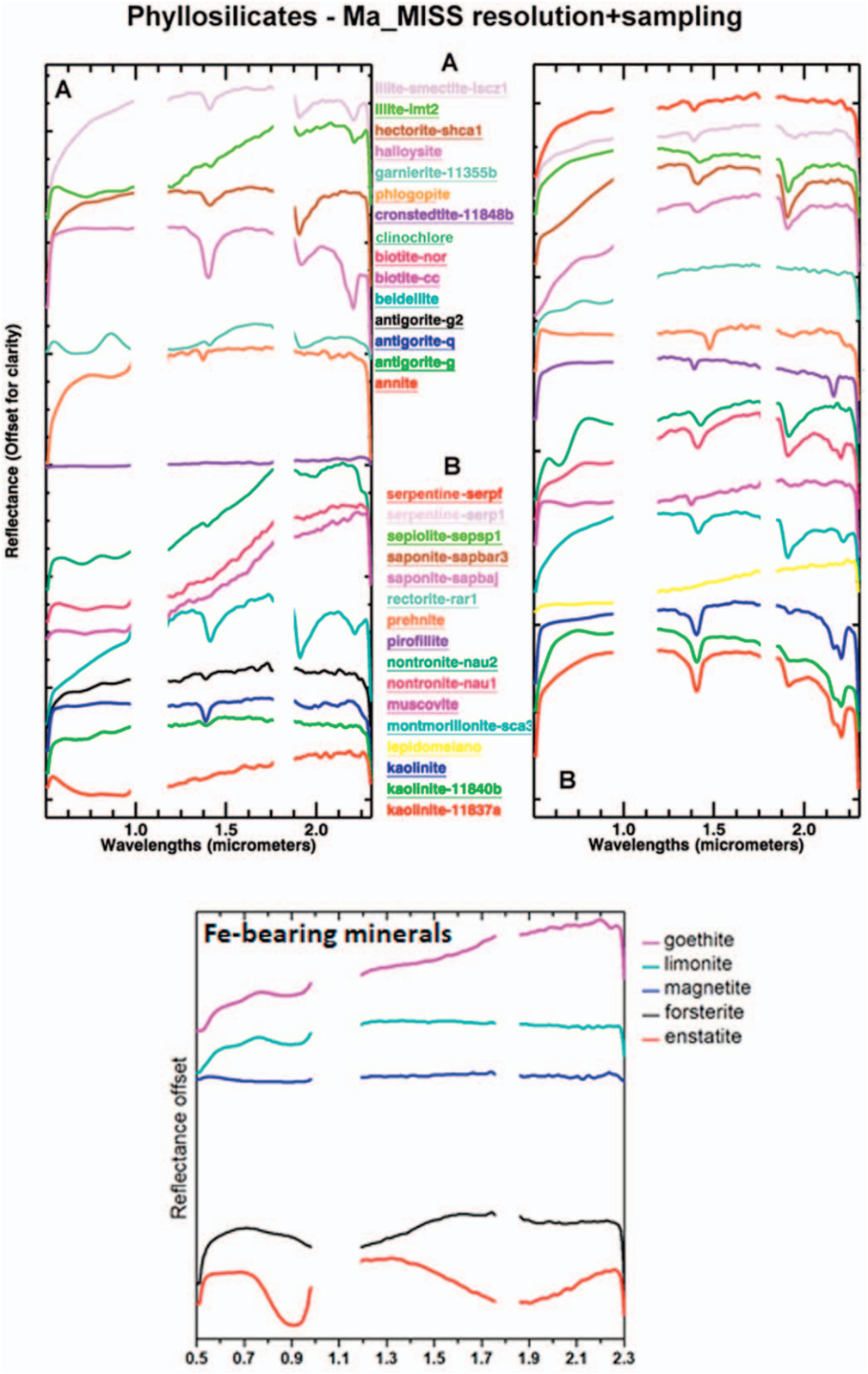


**Figure 7.** Selection of spectra of minerals (top: phyllosilicates; bottom: silicates) acquired with the Ma_MISS breadboard at the IAPS INAF laboratory. Acquisitions have been carried out on mineral powders with the Ma_MISS breadboard laboratory model, and data were subsequently processed to simulate the Ma_MISS FM spectral sampling and resolution. The laboratory spectra are affected by gaps due to the low S/N occurring in the 1.0–1.1 $\mu$m and 1.7–1.8 $\mu$m ranges of the spectrometer (FieldSpec) used in the laboratory. The Ma_MISS instrument is not affected by these gaps.

IAPS_INAF laboratory is reported in Figure 10. Our spectra have also been normalized, in order to have a more immediate comparison.

In the case of Montiferru basalt, the spectra have been acquired at different positions on the slab. Looking at Figure 10, it is evident that the data acquired with Ma_MISS

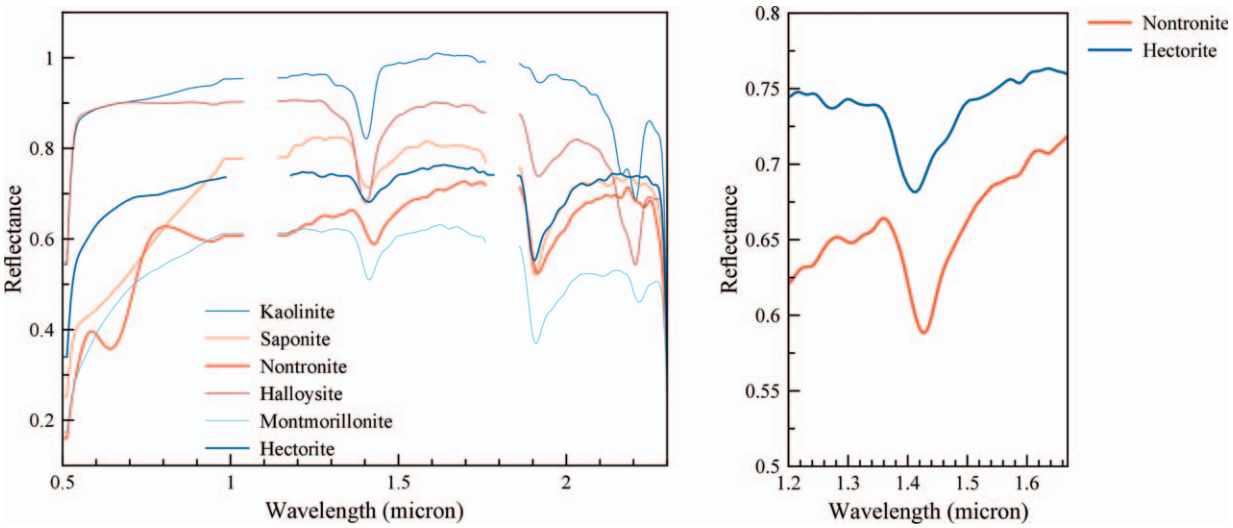


**Figure 8.** Left: spectra of different minerals acquired with the Ma_MISS breadboard and resampled and processed to simulate the Ma_MISS FM spectral sampling and resolution. Right: zoom-in of the region of 1.4 $\mu$m for two phyllosilicates: nontronite (Fe-rich) and hectorite (Mg-rich). The laboratory spectra are affected by gaps due to the low S/N occurring in the 1.0–1.1 $\mu$m and 1.7–1.8 $\mu$m ranges of the spectrometer (FieldSpec) used in the laboratory. The Ma_MISS instrument is not affected by these gaps.

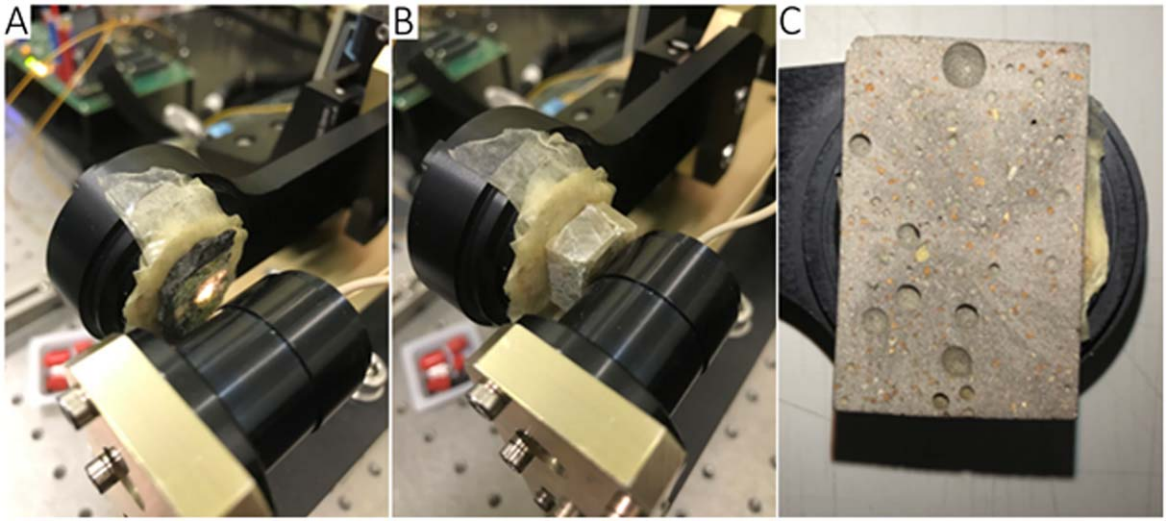


**Figure 9.** (a) Slab of dunite rock; (b) slab of gypsum; (c) slab of Montiferru (Bonàrcado) lava. These pictures were taken during the acquisition with Ma_MISS (panels (a)–(b)) and before the measurements (panel (c)).

FM and those acquired at the INAF laboratory are very similar and all the main spectral features are easily comparable. However, it is also evident that the spectral bands are more pronounced in the case of the data acquired at the INAF laboratory. It must be considered that the two instrumental setups have a very different spatial resolution (smaller area in the case of Ma_MISS) and very different illumination sources in terms of emitted power (5 W Ma_MISS lamp vs. 100 W for the laboratory lamp), so they can investigate differently the single rock-forming minerals. Moreover, the position of the acquired area on the slabs is certainly different in the two measurements (Ma_MISS vs FieldSpec). Being natural samples, the slabs are heterogeneous, and the measurements have acquired portions of the slabs characterized by slightly different spectral characteristics. We were not able to observe exactly the same spots (120 $\mu$m size) that were acquired with the Ma_MISS BB. When the Ma_MISS FM and INAF laboratory spectra are normalized at the same wavelengths, they show very similar behaviors, and the small differences can be ascribed to the differences in the acquisition spots and illumination condition. Looking at the sample of dunite measured with the FieldSpec, it seems that it has both olivine (band centered at 1 $\mu$m) and low Ca-pyroxene (shallow spectral absorption at about 1.9 $\mu$m), while the spectrum obtained with the Ma_MISS flight model only shows olivine in the FOV, being nearly absent in the 1.9 $\mu$m band. These differences can be natural in a xenolith where both minerals occur, though olivine is more numerous.

As for the Montiferru lava (MFEB1) sample, the Ma_MISS and FSpec spectra display a very good match along the spectral range, even if some differences can be seen. The spectra collected on the three points on the slab of Montiferru lava (purple, green, and yellow spectra in Figure 10) are quite similar to each other. The weak absorption feature at 1.9 $\mu$m is due to the presence of some hydrated phase in the sample. The spectrum obtained on the gypsum slab (red spectrum in

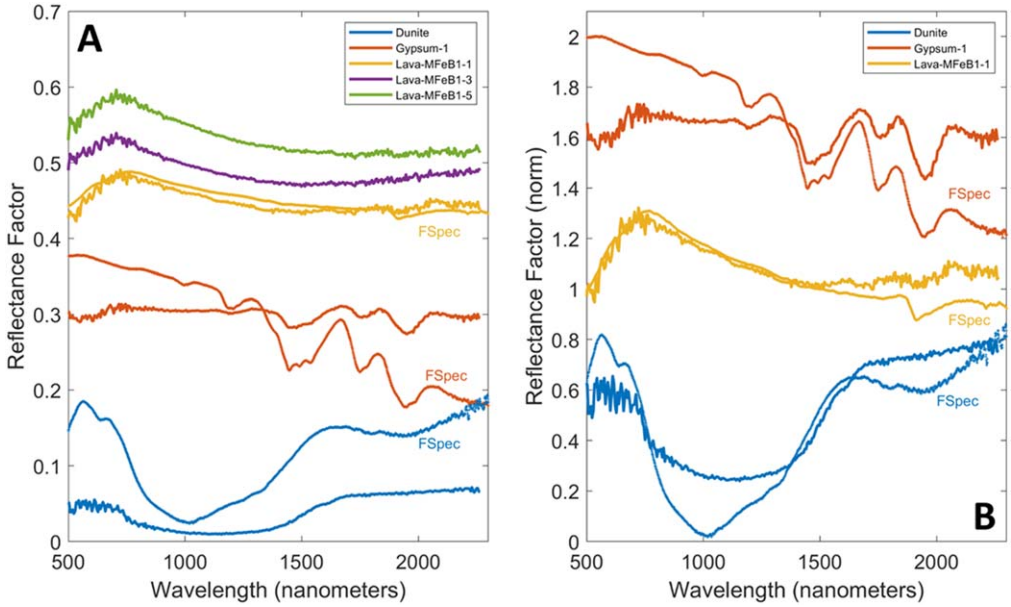


**Figure 10.** (a) Rock/mineral slab spectra acquired with the Ma_MISS flight model during the on-ground calibration campaign; data are compared with spectra acquired on the same samples at the INAF laboratory (labeled FSpec). (b) Rock/mineral slab spectra acquired with the Ma_MISS flight model (cross lines) during the on-ground calibration campaign; data are compared with spectra acquired on the same samples at the INAF laboratory (solid lines). Here the spectra have been normalized at 1450, 1500, and 1700 nm for gypsum, Lava Montiferru MFEB1, and dunite, respectively.

Figure 10) shows all its typical absorption features related to water molecule vibrations. The blue spectrum acquired on the dunite sample shows the wide absorption band (from 0.6 to 1.6 $\mu$m) near 1 $\mu$m typical of olivine. The differences in the spectra acquired with Ma_MISS and with the BB can be ascribed to the acquisition of different spots on the slabs. It was impossible to observe exactly the same spots in the two configurations (BB and flight model), and the spectra can be different because changing positions on the natural samples means acquiring different mineral phases.

The effects of the different spatial resolution have been reported previously (De Angelis et al. 2019), demonstrating that the Ma_MISS instrument allows retrieving spectral information with much greater detail on a submillimeter scale. The smaller spot of Ma_MISS (0.12 mm) allows recognizing different mineralogical phases with size down to about 100 $\mu$m. This capability is extremely useful to recognize the different mineral phases present in the Martian subsurface.

### *4.2. Tests of the Performances with the Extension Rods*

The ExoMars drill is constituted by the main rod (tip drill tool), where the Ma_MISS window and optical head are located, and three extension rods that can be added to achieve the 2 m in depth. Performance tests of the instrument with the different rods were done in Leonardo (Nerviano, MI, Italy) in 2018 October (Figure 11).

We used standard spectral targets (LabSphere WCS-E0, WCS-H0, and WCS-MC), characterized by a flat Lambertian surface with reflectivity around 99% and several absorption features due to a rare Earth material surface coating. These targets were acquired several times in different instrument/drill configurations, starting with the tip drill tool and adding the extension rods consecutively. Measurements were

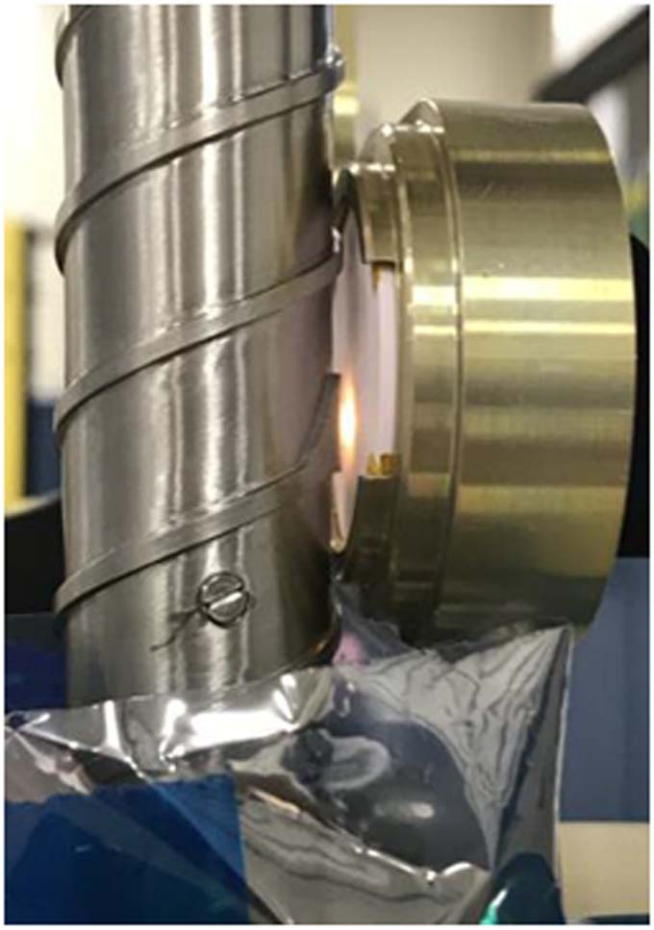

**Figure 11.** Ma_MISS lamp illuminating a spectral target during the measurements on the tip and rods in Leonardo Nerviano (MI).

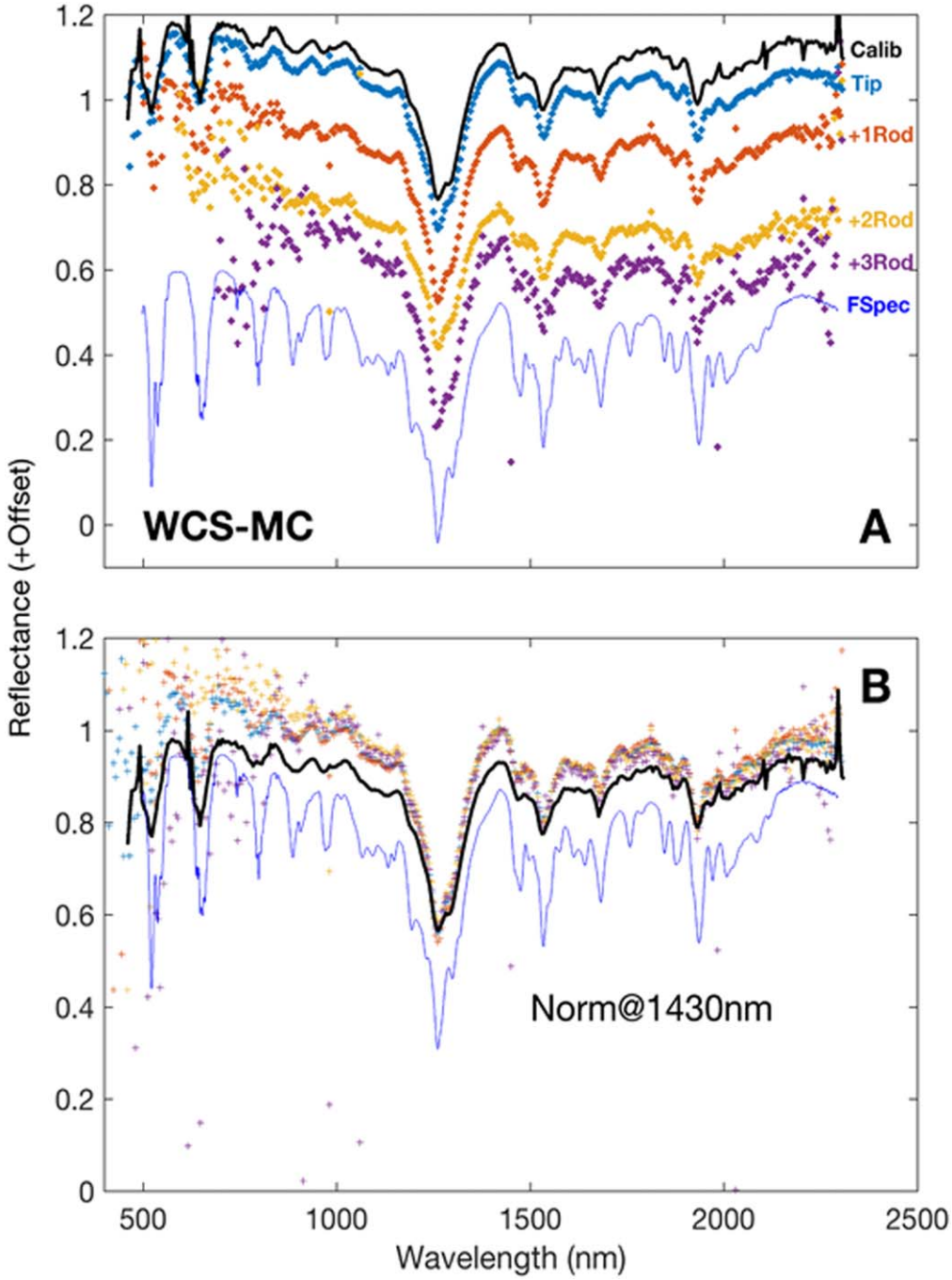


**Figure 12.** WCS-MC standard spectral target (LabSphere©) WCS-MC, acquired with Ma_MISS FM integrated within the drill FM. Spectra have been acquired with the Ma_MISS tip only (thick blue line), and with the extension rods mounted up to three rods (tip + one rod: orange; tip + two rods: yellow; tip + three rods: magenta). The spectrum of WCS-MC acquired during the on-ground calibration campaign (TDet = −50 °C) is shown for comparison (black). The spectrum of WCS-MC measured with FieldSpec at the IAPS laboratory is also shown (thin blue line). In panel (a), the spectra are shifted in reflectance for clarity. In panel (b), the spectra have been normalized at 1430 nm. The spectral resolution of the FieldSpec is about 10 times better with respect to the Ma_MISS one.

performed with the target, instrument, and drill deployment in air, with the detector maintained at a temperature of −25°C. The LabSphere Spectralon 99% was used as a reference target to obtain reflectance spectra. The targets and reference were acquired with the (1) tip, (2) tip + rod 1, (3) tip + rod 1 + rod 2, and (4) tip + rod 1 + rod 2 + rod 3; dark current has been acquired with the lamp off with the same integration times. Due to internal reflection, Ma_MISS also has a ghost signal that must be considered when the calibration is performed: this is a small fraction (about 5% of peak signal) of the lamp light that is reflected by the internal surface of the sapphire window and returns to the spectrometer. In order to calibrate the data in reflectance, the ghost signal also needs to be acquired with the same instrument+drill configuration as for the target and reference (tip and eventually rods). Concerning the dark signal, because it is acquired with the lamp switched off, it is independent of the number of mounted rods.

For the generic $N$ rod configuration, with $N = 0, 1, 2, 3$, the relative calibration in reflectance is as follows:

$$\mathrm{Refl} = \frac{\left[\left(\frac{S_{\mathrm{target}}}{t_{\mathrm{exp}}} - \frac{\mathrm{Dark}}{t_{\mathrm{exp}}}\right) - \left(\frac{S_{\mathrm{ghost}}}{t_{\mathrm{exp}}} - \frac{\mathrm{Dark}}{t_{\mathrm{exp}}}\right)\right]_{\mathrm{Rod}\#N}}{\left[\left(\frac{S_{\mathrm{REF}}}{t_{\mathrm{exp}}} - \frac{\mathrm{Dark}}{t_{\mathrm{exp}}}\right) - \left(\frac{S_{\mathrm{ghost}}}{t_{\mathrm{exp}}} - \frac{\mathrm{Dark}}{t_{\mathrm{exp}}}\right)\right]_{\mathrm{Rod}\#N}},$$

where Refl means reflectance, $S_{\mathrm{target}}$ is for signal from the target, $S_{\mathrm{REF}}$ is for signal from the reference target, $S_{\mathrm{ghost}}$ is the signal coming from the ghost, $T_{\mathrm{exp}}$ is for integration time, and Dark is for the dark signal.

This equation has been used to compute the relative reflectance of the WCS-MC target measured with the tip, one rod, two rods, and three Rods. Because the ghost was only acquired with the tip and the tip + three rods, it was necessary to scale the ghost to the signal corresponding to one and two rods, using the rod transmittance. The transmittance was retrieved as follows: (i) by computing the ratio of the ghost (three rods) to ghost (tip) and then taking the cubic root, and (ii) by computing the ratio of Spectralon99 (one rod) to Spectralon99 (tip).

For each drill configuration the WCS-MC spectrum has been computed as follows:

(1) Tip: the target (WCS-MC), reference (Spectralon99), ghost, and dark were acquired with 2 ms integration time.
(2) Tip + rod1 : the target, reference, and dark were acquired with 1 ms integration time; the ghost was missing for this configuration, so it was necessary to scale the tip-ghost by means of the rod transmittance (T1Rod), that is, multiplying by T1Rod.
(3) Tip + rod 1 + rod 2: the target, reference, and dark were acquired with 2 ms integration time; the ghost was missing for this configuration, so it was necessary to scale the tip-ghost by means of the rod transmittance (T1Rod), that is, multiplying by T1Rod*T1Rod.
(4) Tip + rod 1 + rod 2 + rod 3: the target, ghost, and dark were measured in Wide mode. The signal was acquired with an integration time of 9 ms (spectral pixel #55 to #127), 5 ms (pixel #128 to #326), and 8 ms (pixel #327 to #418). These pixel ranges correspond to the wavelengths 380–770 nm, 770–1830 nm, and 1830–2300 nm. Because the Spectralon acquisition was missing for this drill configuration, the reference measured with the tip + two rods was used and scaled by means of the rod transmittance.

The relative reflectance of WCS-MC retrieved with the different drill configurations is shown in Figure 12(a), with vertical offset for clarity. The data are also compared with the spectrum measured during the on-ground Calibration Campaign (2018 April at Leonardo, Florence); on that occasion the data were acquired with the instrument in TVC and the detector cooled down at the nominal temperature of −50°C, and thus they are characterized by a higher S/N. The spectra are also compared with the measurement performed in the laboratory at INAF-IAPS with the ASD-FieldSpec4 commercial spectrometer, characterized by high spectral resolution (3–8 nm) in the 0.35–2.5 $\mu$m range. In Figure 12(b), the spectra have been normalized at 1430 nm in order to highlight any differences arising between the different drill configurations.

Comparing the data acquired with the tip only and those acquired using the different rods + the tip, it is evident that there is a degradation of the quality of the spectra when increasing the numbers of the rods, as expected. If we look at the data obtained using only one rod + the tip, the spectra are extremely similar and we can note only an increase of the noise at the spectral range borders.

Adding more rods, the noise increases especially at wavelengths shorter than 800 nm. This trend is expected owing to the instrumental response that is worst in the visible part of the wavelength range. The NIR part of the spectral range is much less affected by the loss of signal given to the additional rods: the spectral features present in that range can be easily recognized and measured.

## 5. Conclusions

The Ma_MISS instrument has been designed to provide hyperspectral data of boreholes excavated by the ExoMars drill. All the measurements done with the Ma_MISS BB and the flight instrument confirm that Ma_MISS spectral range, resolution, and imaging capabilities are suitable for the characterization of the first 2 m of the Martian subsurface environment. Ma_MISS recognizes all the major spectral features of the clays, basaltic rocks, and minor phases expected to be pervasive at the landing site.

The spatial distribution of the mineralogical composition of the rocks exposed in the borehole wall is associated with the sequences of processes that put these materials in place and possibly altered them afterward, characterizing the habitats found in the stratigraphic record, indicating which ones of them are the most suitable to hold traces of life. The high spatial resolution on the borehole wall is such that grains of about 100 $\mu$m can be distinguishable in the matrix observed by Ma_MISS. Thus, it should be possible to acquire spectra on monominerals. The usage of the drill rods, up to 2 m depth, does not impact the Ma_MISS ability to detect mineral phases in their stratigraphic context, permitting the full characterization of the stratigraphic columns from which the samples will be collected. Moreover, Ma_MISS can is key to determine which give important information on the candidate samples that will be delivered to the rover's analytical laboratory, providing criteria for their selection and further analyses.

An excellent understanding of the composition and distribution of subsurface materials at the rover landing site is vital in our efforts to establish whether life might have occurred on Mars and whether the planet subsurface may have preserved biosignatures of any such life.

We thank the European Space Agency (ESA) for the ExoMars Project, ROSCOSMOS and Thales Alenia Space for rover development, and Italian Space Agency (ASI) for funding and fully supporting Ma_MISS experiment (grant ASI-INAF No. 2017-48-H.0). We thank two anonymous referees for their helpful comments on the manuscript.

## ORCID iDs

M. C. De Sanctis https://orcid.org/0000-0002-3463-4437
F. Altieri https://orcid.org/0000-0002-6338-8300
B. Ehlmann https://orcid.org/0000-0002-2745-3240
M. Formisano https://orcid.org/0000-0003-3236-1604

## References

Allen, M., Sherwood Lollar, B., Runnegar, B., et al. 2006, EOSTr, 87, 433
Altieri, F., De Sanctis, M. C., Ferrari, M., et al. 2021, LPSC, 52, 2040

Anderson, J. H., Jr., & Wickersheim, K. A. 1964, SurSc, 2, 252
Arvidson, R. E., Bell, J. F., Bellutta, P., et al. 2010, JGRE, 115, E00F03
Arvidson, R. E., Poulet, F., Bibring, J.-P., et al. 2005, Sci, 307, 1591
Banin, A., Clark, B. C., & Wanke, H. 1992, in Mars, ed. H. H. Kieffer et al. (Tucson, AZ: Univ. Arizona Press), 594
Bibring, J.-P., Arvidson, R. E., Gendrin, A., et al. 2007, Sci, 317, 1206
Bishop, J., Parente, M., Weitz, C. M., et al. 2009, JGRE, 114, E00D09
Bibring, J.-P., Langevin, Y., Mustard, J. F., et al. 2006, Sci, 312, 400
Bibring, J.-P., Soufflot, A., Berthé, M., et al. 2004, in ESA SP-1240, Mars Express: The Scientific Payload, ed. A. Wilson (Noordwijk: ESA), 37
Bishop, J. L., Dobrea, E. Z. N., McKeown, N. K., et al. 2008, Sci, 321, 830
Bishop, J. L., Tirsch, D., Tornabene, L., et al. 2013, JGRE, 118, 487
Bristow, T. F., Rampe, E. B., Achilles, C. N., et al. 2018, SciA, 4, eaar3330
Brossier, J., Altieri, F., De Sanctis, M. C., et al. 2022, Icar, in press
Brossier, J., Altieri, F., De Sanctis, M. C., et al. 2022, LPSC, 53, 1288
Carter, J., Poulet, F., Bibring, J.-P., Mangold, N., & Murchie, S. 2013, JGRE, 118, 831
Carter, J., Quantin, C., Thollot, P., et al. 2016, LPSC, 47, 2064
Chemtob, S. M., Nickerson, R. D., Morris, R. V., Agresti, D. G., & Catalano, J. G. 2015, JGRE, 120, 1119
Clark, R. N., King, T. V. V., Klejwa, M., et al. 1990, JGR, 95, 12653
De Angelis, S., Carli, C., Tosi, F., et al. 2019, Icar, 317, 388
De Angelis, S., De Sanctis, M. C., Ammannito, E., et al. 2014, P&SS, 101, 89
De Angelis, S., De Sanctis, M. C., Ammannito, E., et al. 2015, P&SS, 117, 329
De Angelis, S., Manzari, P., De Sanctis, M. C., et al. 2017, P&SS, 144, 1
De Sanctis, M. C., Altieri, F., Ammannito, E., et al. 2017, AsBio, 17, 612
Ehlmann, B. L., & Edwards, C. S. 2014, AREPS, 42, 291
Ehlmann, B. L., Mustard, J. F., Clark, R. M., et al. 2011b, CCM, 590, 359
Ehlmann, B. L., Mustard, J. F., Murchie, S. L., et al. 2011a, Natur, 479, 53
Ehlmann, B. L., Mustard, J. F., Swayze, G. A., et al. 2009, JGRE, 114, E00D08
Eigenbrode, J. L., Summons, R. E., Steele, A., et al. 2018, Sci, 360, 1096
Ferrari, M., De Angelis, S., De Sanctis, M. C., et al. 2022, EPSC, 14, 1339
Ferrari, M., De Angelis, S., De Sanctis, M. C., et al. 2021, LPSC, 52, 1914
Formisano, M., De Sanctis, M. C., Federico, C., et al. 2021, AdAst, 2021, 9924571
Gaffey, S. J. 1986, AmMin, 71, 151
Gaffey, S. J. 1987, JGR, 92, 1429
Gellert, R., & Yen, S. 2019, in Remote Compositional Analysis: Techniques for Understanding Spectroscopy, Mineralogy, and Geochemistry of Planetary Surfaces, ed. J. Bishop, J. Bell, III, & J. Moersch (Cambridge: Cambridge Univ. Press), 555
Gendrin, A., Mangold, N., Bibring, J.-P., et al. 2005, Sci, 307, 1587
Gorevan, S. P., Myrick, T., Davis, K., et al. 2003, JGRE, 108, 8068
Hanley, J., Chevrier, V. F., Barrows, R. S., Swaffer, C., & Altheide, T. S. 2015, JGRE, 120, 1415
Hunt, G. R. 1977, Geop, 42, 501
Hunt, G. R., & Ashley, R. P. 1979, Economic Geology, 74, 1613
Hunt, & Salisbury 1971, Mod Geol., 2, 195
Hurowitz, J. A., Grotzinger, J. P., Fischer, W. W., et al. 2017, Sci, 356, aah6849
Ivanov, M. A., Slyuta, E. N., Grishakina, E. A., & Dmitrovskii, A. A. 2020, SoSyR, 54, 1
Kminek, G., & Bada, J. L. 2006, EPSL, 245, 1
Kounaves, S. P., Hecht, M. H., Kapit, J., et al. 2010, GeoRL, 37, L09201
Langevin, Y., Poulet, F., Bibring, J.-P., & Gondet, B. 2005, Sci, 307, 1584
Lichtenberg, K., Arvidson, R. E., Morris, R. V., et al. 2010, JGRE, 115, E00D17
Liu, Y., Glotch, T., Scudder, N. A., et al. 2016, JGRE, 121, 2004
Loizeau, D., Mangold, N., Poulet, F., et al. 2007, JGRE, 112, E08S08
Makarov, I. E., & Ponomarev, A. V. 2017, in Ionizing Radiation Effects and Applications, ed. B. Djezzar (London: InTech Open Books)
Mandon, L., Parkes, B. A., Quantin-Nataf, C., et al. 2021, AsBio, 21, 464
McEwen, A. S., Banks, M. E., Baugh, N., et al. 2010, Icar, 205, 2
McEwen, A. S., Eliason, E. M., Bergstrom, J. W., et al. 2007, JGRE, 112, E05S02
McKeown, N. K., Bishop, J. L., Noe Dobrea, E. Z., et al. 2009, JGRE, 114, E00D10
McNeil, J. D., Fawdon, P., Balme, M. R., & Coe, A. L. 2021, JGRE, 126, e06775
McSween, Y. H., Murchie, S. L., Crisp, J. A., et al. 1999, JGR, 104, 8679
Milliken, R. E., Swayze, G. A., Arvidson, R. E., et al. 2008, Geo, 36, 847
Molina, A., López, I., Prieto-Ballesteros, O., et al. 2017, Icar, 293, 27,
Morris, R. V., Agresti, D. G., Lauer, H. V., et al. 1989, JGR, 94, 2760,
Morris, R. V., Schröder, C., Klingelhöfer, G., & Agresti, D. G. 2019, in Remote Compositional Analysis: Techniques for Understanding Spectroscopy, Mineralogy, and Geochemistry of Planetary Surfaces, ed. J. Bishop, J. Bell, III, & J. Moersch (Cambridge: Cambridge Univ. Press), 538
Morris, R. V., Golden, D. C., & Bell, J. F. 1997, JGR, 102, 9125
Morris, R. V., Golden, D. C., Bell, J. F., III, et al. 1993, GeCoA, 57, 4597
Morris, R. V., Vaniman, D. T., Blake, D. F., et al. 2016, PNAS, 113, 7071
Murchie, S. L., Arvidson, R., Bedini, P., et al. 2007, JGRE, 112, E05S03
Murchie, S. L., Mustard, J. F., Ehlmann, B. L., et al. 2009, JGRE, 114, E00D06
Mustard, J. F., Murchie, S. L., Pelkey, S. M., et al. 2008, Natur, 454, 305
Noe Dobrea, E. Z., Bishop, J. L., McKeown, N. K., et al. 2010, JGRE, 115, E00D19
Poulet, F., Bibring, J. -P., Mustard, J. F., et al. 2005, Natur, 438, 623
Quantin-Nataf, C., Carter, J., Mandon, L., et al. 2021, AsBio, 21, 345
Rapin, W., Chauviré, B., Gabriel, T. S. J., et al. 2018, JGRE, 123, 1955
Rossman, G., & Ehlmann, B. 2019, in Remote Compositional Analysis: Techniques for Understanding Spectroscopy, Mineralogy, and Geochemistry of Planetary Surfaces, ed. J. Bishop, J. Bell, III, & J. Moersch (Cambridge: Cambridge Univ. Press), 3
Sherwood Lollar, B., Lacrampe-Couloume, G., Slater, G. F., et al. 2006, ChGeo, 226, 328
Singer, R. B. 1982, JGR, 87, 10,159
Soderblom, L. A. 1992, in Mars, ed. H. H. Kieffer et al. (Tucson, AZ: Univ. Arizona Press), 557
Squyres, S. W., Arvidson, R. E., Bell, J. F., et al. 2004, Sci, 306, 1698
Sullivan, R., Anderson, R., Biesiadecki, J., Bond, T., & Stewart, H. 2011, JGR, 116, E02006
Tanaka, K. L., Skinner, J. A., Dohm, J. M., et al. 2014, U.S.G.S. Scientific Investigations Map, 3292
Tinivelli, P., De Angelis, S., Ferrari, M., et al. 2018, in 5th IEEE International Workshop on Metrology for AeroSpace (MetroAeroSpace) (Piscataway, NJ: IEEE), 128
Treiman, A. H., Morris, R. V., Agresti, D. G., et al. 2014, AmMin, 99, 2234
Vago, J. L., Westall, F., Pasteur Instrument Team, et al. 2017, AsBio, 17, 471
Vaniman, D. T., Bish, D. L., Ming, D. W., et al. 2013, Sci, 343, 1243480
Vaniman, D. T., Martínez, G. M., Rampe, E. B., et al. 2018, AmMin, 103, 1011
Wang, A., Haskin, L. A., Squyres, S. W., et al. 2006, JGRE, 111, E02S17
Wang, A., Jolliff, B. L., & Connor, K. 2016, JGRE, 121, 678
Wellington, D. F., Bell, J. F., Johnson, J. R., et al. 2017, AmMin, 102, 1202
Wilson, J. T., Eke, V. R., Massey, R. J., et al. 2017, Icar, 299, 148
Yung, Y. L., Russell, M. J., & Parkinson, C. D. 2010, JCos, 5, 1121
Zacny, K., & Cooper, G. 2006, P&SS., 54, 345